CAMBRIDGE
UNIVERSITY PRESS

Research Article

Spectro-polarimetric study to constrain accretion-ejection properties of MCG-5-23-16 using *IXPE* and *NuSTAR* observations

Santanu Mondal[1] ⬤, Rwitika Chatterjee[2], Vivek K. Agrawal[2] and Anuj Nandi[2]

[1]Indian Institute of Astrophysics, Koramangala, Bengaluru, India and [2]Space Astronomy Group, ISITE Campus, U. R. Rao Satellite Center, ISRO, Bengaluru, India

Abstract

We conducted a study on the X-ray polarisation properties of MCG-5-23-16 by analysing long-term monitoring data from *NuSTAR* jointly with *IXPE* observations made in May and November 2022. The re-analysis of *IXPE* data gives model-dependent polarisation degree, PD (%) = 1.08 ± 0.66 in the energy band 2–8 keV, which agrees with previous studies within error bars. The model-independent analysis of PD poses an upper limit of ≤ 3.8 (1σ level) for the same energy band. The observed upper limit of PD, along with broadband spectral analysis (2–79 keV) using an accretion-ejection based model, allowed us to derive the corona geometry (i.e. radius and height) and the accretion disc inclination ($\sim 33°$). Additional *NuSTAR* observations were also analysed to gain insights into the accretion flow properties of the source and to estimate the expected polarisation during those epochs with PD $\sim 4.3\%$. The radius and height of the corona varies between $28.2 \pm 3.1 - 39.8 \pm 4.6 \, r_s$ and $14.3 \pm 1.7 - 21.4 \pm 1.9 \, r_s$ respectively, with a mass outflow rate from the corona measuring $0.14 \pm 0.03 - 0.2 \pm 0.03$ Eddington rate ($\dot{m}_{Edd}$). The estimated PD values were nearly constant up to a certain radial distance and height of the corona and then decreased for increasing corona geometry. The spectral analysis further provided an estimate for the mass of the central black hole $\sim 2 \times 10^7 \, M_\odot$ and the velocity of the outflowing gas $\sim 0.16 - 0.19c$. A comparative broadband spectral study using reflection-based models estimates the disc inclination between $\sim 31° \pm 8° - 45° \pm 7°$, and yields an expected PD of 3.4–6.0%. We also found a weak reflection fraction and a less ionised distant reflecting medium. The expected PD measured using accretion-ejection and reflection models is less compared to the expected PD measured for a given disc inclination of 45°. Our modelling of the disc-corona-outflows and polarisation connection can be extended and validated with data from the recently launched *XPoSat*, India's first X-ray Polarimeter Satellite, offering potential applications to other sources.

Keywords: Accretion disc; galaxies:active; galaxies: Seyfert; polarisation; X-rays: individual: MCG-5-23-16

(Received 5 March 2024; revised 31 July 2024; accepted 8 August 2024)

1. Introduction

Recent launches of *Imaging X-ray Polarimetry Explorer* (IXPE; Weisskopf et al. 2016) and *X-ray Polarimeter Satellite* (XPoSat)[a] Missions have renewed interest in measuring X-ray polarisation from diverse astrophysical systems, in particular from accreting black hole (BH) systems of all scales. Accreting matter puffs up at the inner region of the disc, which not only upscatters soft photons through inverse Comptonization (Sunyaev & Titarchuk 1980; Haardt & Maraschi 1993; Chakrabarti & Titarchuk 1995; Done, Gierliński, & Kubota 2007; Mondal & Chakrabarti 2013; Iyer, Nandi, & Mandal 2015, and references therein) but also polarises the radiation depending on its thermodynamic properties, geometry, and inclination (Connors, Piran, & Stark 1980; Sunyaev & Titarchuk 1985). Therefore, the measurement of polarisation angle (PA) and degree (PD) depends on both corona (Compton cloud) properties as well as the photon energy. Additionally, the presence of outflows from the disc can also produce significant polarisation

due to scattering effects (Begelman & McKee 1983). The dependence of PD and PA on the optical depth and disc inclination was studied using different geometry of the corona in detail (Dovčiak et al. 2008; Li, Narayan, & McClintock 2009; Schnittman & Krolik 2010, and references therein). Therefore, if the corona properties of a system is well constrained, the PD can be estimated or the vice-versa. Hence, the spectro-polarimetric studies using broadband data may shed more light on the measurement of polarisation and the environment of the corona around BHs.

MCG-5-23-16 is a Seyfert 1.9 galaxy (Veron et al. 1980) located at redshift $z = 0.00849$ (Wegner et al. 2003). The source is relatively bright in X-rays with $F_{2-10} = 7 - 10 \times 10^{-11}$ erg cm^{-2} s^{-1} (Mattson & Weaver 2004) and characterised by moderate neutral absorption ($N_H \sim 10^{22}$ cm^{-2}). It has been extensively studied in the X-ray band to estimate corona properties and spectral high-energy cut-off using *INTEGRAL* and *NuSTAR* observations (Beckmann et al. 2008; Molina et al. 2013; Baloković et al. 2015; Zoghbi et al. 2017).

Furthermore, the X-ray spectrum of this source showed the presence of a soft excess and complex Fe Kα emission with broad and asymmetric narrow line features in *ASCA* (Weaver et al. 1997), *BeppoSAX*, *Chandra*, and *XMM-Newton* (Dewangan, Griffiths, & Schurch 2003; Balestra, Bianchi, & Matt 2004; Braito et al. 2007; Liu, Zoghbi, & Miller 2024) observations. It indicates the presence of two reflectors, one for a narrow core at 6.4 keV and the other for

the broad component, possibly originating closer to the BH. Later, the broad line was explored with *Suzaku* (Reeves et al. 2007) and reported that the inner radius of the disc is 20 r_s that originated the line, where $r_s = 2GM_{BH}/c^2$ is the Schwarzschild radius, with an inclination 50°. Additionally, an absorption feature at 7.7 keV was unveiled in these data, pointing to the possible presence of ionised iron outflowing at $\sim 0.1c$. Recently, Serafinelli et al. (2023) estimated the disc inclination of 41° from the broad Fe Kα line study using *NuSTAR* observations. Marinucci et al. (2022) estimated the disc inclination $48°^{+12}_{-8}$ from broad Fe Kα line profile. The disc inclination also found to lie between $40° - 50°$ (see also Weaver & Reynolds 1998). The mass of the central supermassive BH (SMBH) is 2×10^7 M$_\odot$ derived independently from both X-ray variability (Ponti et al. 2012) and infrared lines (Onori et al. 2017).

Along with spectral and timing studies, X-ray polarisation provides an independent tool to constrain the accretion properties and coronal geometry. It has been reported that the polarisation is extremely sensitive to the geometry of the radiation emitting region and the photon field (Schnittman & Krolik 2010; Beheshtipour, Krawczynski, & Malzac 2017; Tamborra et al. 2018, and references therein). To constrain the source coronal geometry, MCG-5-23-16 was targeted by two pointings in 2022 with IXPE.

The joint analysis of *XMM-Newton*, *NuSTAR*, and *IXPE* observations in May 2022 by Marinucci et al. (2022) obtained a 4.7% (at 99% confidence level) upper limit for the polarisation degree (PD) in the 2–8 keV energy band and ruled out the slab geometry of the corona. Authors also found a hint of alignment between the polarisation angle and the accretion disc spin axis. Later, Tagliacozzo et al. (2023) analysed the *IXPE* data from both May and November 2022 epochs in coordination with *NuSTAR* and estimated the upper limit of PD to be 3.2 % (at 99% confidence level for one parameter of interest). Their preferred polarisation angle in the $\sim 50°$ direction may hint that the polarisation of the primary emission is aligned with the Narrow Line Region, which was observed at $\sim 40°$ position angle in Hubble Space Telescope's WFPC2 images (Ferruit, Wilson, & Mulchaey 2000) and therefore, parallel to the accretion disc axis, similar to what was found in NGC 4151 (Gianolli et al. 2023). Such alignments may contribute to the polarisation measurement just below detection. The authors further compared their observed estimations with Monte Carlo simulations of the expected polarisation properties for different geometries of the corona and disfavoured the lamppost and cone-shaped corona.

Therefore, we see that polarisation can be used as a probe to understand the geometry of the corona and accretion-ejection behaviour around the central SMBH. The continuum models applied to study the spectral properties of the source MCG-5-23-16 mostly take into account radiative transfer processes. However, to date, no physically motivated accretion-ejection based models have been directly employed to fit and understand the polarisation properties with the corona geometry or accretion flow parameters. In this work, we have re-analysed the *IXPE* observations to confirm the previous studies jointly with *NuSTAR* data for both epochs (May and November 2022). Further, other data sets available in the *NuSTAR* archive were also analysed to constrain the corona properties and to predict the polarisation behaviour. Moreover, we have also estimated the mass outflow rate for all epochs, that connect the disc-corona-outflow geometry with polarisation from a single framework.

Table 1. Log of observations of MCG-5-23-16. The * denotes data used for joint spectro-polarimetric analysis.

Obs. Id.	Exp. (ks)	Epoch	Start Date	End Date
IXPE				
01003399	436	I1	2022-05-14	2022-05-31
02003299	641	I2	2022-11-06	2022-11-23
NuSTAR				
60701014002*	84	N1	2022-05-21	2022-05-23
90801630002*	86	N2	2022-11-11	2022-11-12
60001046008	221	N3	2015-03-13	2015-03-18
60001046006	98	N4	2015-02-21	2015-02-23
60001046004	210	N5	2015-02-15	2015-02-20
60001046002	160	N6	2013-06-03	2013-06-07
10002019001	34	N7	2012-07-11	2012-07-11

The paper is organised as follows: in Section 2, we discuss the observation and data reduction procedure. In Section 3, we describe the spectro-polarimetric data analysis results, and finally, we draw our conclusions in Section 4.

2 Observation and data reduction

Over the past decade, MCG-5-23-16 was observed by *NuSTAR* (Harrison et al. 2013), spanning from 2012 to 2022. Most recently, the source was observed in May and November 2022 by *IXPE* (Weisskopf et al. 2016), launched on 2021 December 9, consisting of three Wolter-I telescopes, with 3 units of polarisation-sensitive imaging X-ray detector units (DUs) at the respective foci. We used all archival data from both observatories for this source and analysed them. The observation log is given in Table 1.

IXPE provides Level-2 data, which we cleaned and calibrated using standard FTOOLS tasks with the latest calibration files (CALDB 20230526) available in *IXPE* database. A circular region centred at the source of radius 60″ (see Tagliacozzo et al. 2023, for details) is used for all detectors. A source-free background region of radius 100″ is used to produce background subtracted spectra for I, Q, and U Stokes for all three DUs. Additionally, we applied a weighting scheme, STOKES = NEFF (Di Marco et al. 2022) in XSELECT to generate the final Stokes spectra in the 2–8 keV energy band.

The *NuSTAR* data were extracted using the standard NUSTARDAS v1.3.1[b] software. We ran a NUPIPELINE task to produce cleaned event lists and NUPRODUCTS along with CALDB version 20231121 to generate the spectra. We used a region of 25″ for the source and 40″ for the background using DS9 (Joye & Mandel 2003). The data were grouped with a minimum of 30 counts in each bin using *grppha* command. For the analysis of each epoch of observation, we used the data of both *IXPE* and *NuSTAR* in the energy range of 2–8 and 3–79 keV. We used XSPEC[c] (Arnaud 1996) version 12.12.0 for spectral analysis. The hydrogen column density for Galactic absorption set fixed to 7.8×10^{20}cm^{-2} (HI4PI Collaboration et al. 2016; Kalberla et al. 2005) during the spectral fitting throughout.

Table 2. Results of model-independent polarimetric analysis in the 2–8 keV band.

Parameter	I1	I2
Q/I (%)	0.27 ± 1.26	-0.15 ± 1.16
U/I (%)	1.33 ± 1.26	1.10 ± 1.16
PD (%)	1.36 ± 1.26	1.11 ± 1.16
PA (%)	39.34 ± 26.56	48.94 ± 29.79
MDP_{99} (%)	3.83	3.50

3. Data analysis and results

3.1 Model-independent and model-dependent IXPE analysis

The processed Level-2 data were used for polarimetric analysis, using IXPEOBSSIM software v30.0.0 (Baldini et al. 2022). Source and background events were extracted using XPSELECT task. We obtained the polarisation parameters in the entire *IXPE* band of 2–8 keV using the model-independent PCUBE algorithm of the XPBIN task (Kislat et al. 2015). Although, there are reports in the literature on the estimation of polarisation, here we have re-done the analysis for the sake of completeness.

The results of our model-independent polarimetric analysis for the two epochs are summarised in Table 2. We obtain only upper limits of the PD for both epochs (below the minimum detectable polarisation at the 99% level). The measured PD and PA in 2–8 keV for the two epochs (I1 and I2) are shown in Fig. 1 along with the contours. The dashed lines correspond to PCUBE contours with 1σ (blue), 2σ (red), 3σ (green) levels. The PD upper limit (99% confidence level) is 3.8% and 3.5% in epochs I1 and I2 respectively. Our estimated upper limit of PD in I2 is consistent with the literature, however, in I1 is lower (Marinucci et al. 2022; Tagliacozzo et al. 2023).

Further, we also performed a spectro-polarimetric model-dependent fit (Strohmayer 2017) using a phenomenological model, consisting of an absorbed CUTOFFPL convolved with a constant polarisation POLCONST which reads in XSPEC as CONST*ZTBABS*POLCONST*CUTOFFPL. The CUTOFFPL model has two spectral parameters, viz. cutoff energy (E_{cut}) and photon index (Γ). The Stokes spectra for all three DUs in the energy band 2–8 keV are fitted simultaneously. A wilm abundance (Wilms, Allen, & McCray 2000) is used throughout the analysis. Since the determination of hydrogen column density may not be reliable owing to the lower energy limit of *IXPE* or *NuSTAR*, we freeze the value of intrinsic N_H to 2.1×10^{22} cm^{-2}, which is the average value determined from *Chandra* observations from 2000 to 2020 (Liu et al. 2024) and the Galactic N_H fixed to 7.8×10^{20} cm^{-2}.

We began by leaving all the spectral and polarimetric parameters to vary freely. We found that the obtained values of PD and PA are highly sensitive to the values of the spectral parameters. Keeping in mind the limited energy band and the spectral sensitivity of *IXPE*, we turned to simultaneous *NuSTAR* observations for obtaining robust spectral fits. In addition to the CUTOFFPL model, the *NuSTAR* data also required an emission feature at the Fe K line energy for a good fit. The full model reads in XSPEC as ZTBABS*(GAUSS+CUTOFFPL), which returned cutoff energy ~ 120 keV, which is consistent with the previous findings by Marinucci et al. (2022) and Tagliacozzo et al. (2023).

Subsequently, we re-did the *IXPE* fits by freezing the values of E_{cut} and Γ to the best-fit values from the *NuSTAR* fit of the respective epoch, which is expected to give a more robust estimation of PD and PA. Note that the addition of a Gaussian line and reflection component neither improves the quality of the fit nor affects the value of the polarisation parameters, hence we did not include these two components while fitting the *IXPE* data. We obtain good fits for I1 and I2 using this model, with $\chi^2_{red} = 0.99$ and 0.92 respectively. We determine the PA = $36.3° \pm 19.4°$ and $72.9° \pm 23.8°$ and the PD (%) = 1.72 ± 1.08 and 1.21 ± 0.89 for the epochs I1 and I2 respectively. However, since the polarisation measurements have a low significance, their values as well as their apparent variation across the epochs should be interpreted with caution. The confidence contours from the model-dependent analysis are shown in Fig. 1. The model-dependent polarimetric results are summarised
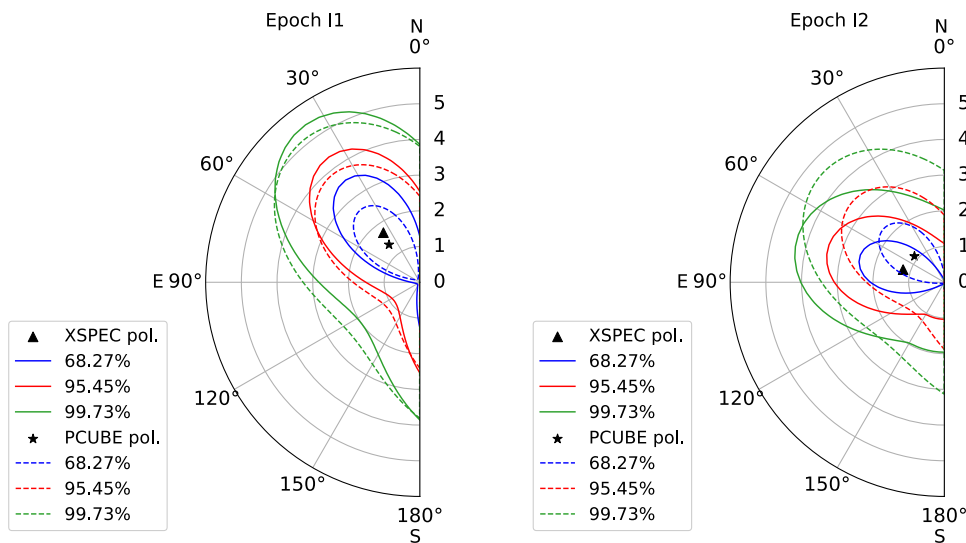

Figure 1. XSPEC (solid lines) and PCUBE (dashed lines) contour plots between polarisation degree PD and angle PA for May (I1; left) and November (I2; right) epochs in 2022. The blue, red, and green contours denote 1σ, 2σ, and 3σ confidence levels. See the text for details.

Table 3. All Stokes spectra for all three DUs of *IXPE* are fitted using `ZTBABS∗POLCONST∗CUTOFFPL` model. The best-fitted parameters of the model-dependent polarimetric analysis are summarised here. All errors are estimated at the 1σ level. The N_H value is frozen to 2.1×10^{22} cm^{-2}.

Parameters	I1	I2	(I1+I2)
PD (%)	1.72 ± 1.08	1.21 ± 0.89	1.08 ± 0.66
PA (°)	36.3 ± 19.4	72.9 ± 23.8	55.6 ± 19.1
Γ	1.66	1.64	1.98 ± 0.02
E_{cut} (keV)	122.2	124.2	123
χ^2/dof	1 312/1 330	1 231/1 330	2 572/2 659

in Table 3. Note that it was mentioned in Tagliacozzo et al. (2023) that the model-dependent contours match with the PCUBE contours. However, for I2, we found a small difference between the PA obtained using the two approaches, and the possible reason for this is not clear yet.

Further, since the PD measurements for both epochs have a low significance (from both model-dependent and model-independent approaches), we attempt to fit the two epochs simultaneously seeking a more significant polarisation estimation. Since the E_{cut} and Γ values obtained from the *NuSTAR* fits do not vary significantly, we tie these values across I1 and I2. Then, we perform the simultaneous fit by constraining them across the epochs. A constant multiplicative factor has been included in the model to account for the cross-calibration across DUs as well as flux changes across epochs. The simultaneously fitted PD is $\sim$10–40% less than the individual epochs and the PA is nearly the mean of the individual analysis since it is done under the assumption that the polarisation characteristics across the two epochs do not differ significantly. The model parameters are summarised in Table 3.

3.2 Spectral analysis of IXPE and NuSTAR

We performed a broadband spectroscopic analysis combining the 2–8 keV *IXPE* spectra and the 3–79 keV *NuSTAR* spectra from May and November 2022. The broadband energy range (2–79 keV) covered by the spectra of MCG-5-23-16 showed a broad Fe K line and a Compton hump above 10 keV. A Gaussian component was required which was free to vary, however, the line energy fitted at $\sim$ 6.3 keV for all observations.

As discussed earlier, the spectra showed the presence of another component that produces the excess emission, which can either be due to reflection (Done, Gierliński, & Kubota 2007) or a signature of mass loss (Chakrabarti 1999) from the corona region. Therefore, we have used two different sets of models one is the accretion-ejection based `JeTCAF` model (Mondal & Chakrabarti 2021), and the others are reflection-based `pexrav` (Magdziarz&Zdziarski 1995) and `relxillCp` models (Dauser et al. 2014; Garcia et al. 2014). Additionally, we have analysed all the *NuSTAR* archival data for the source MCG-5-23-16 covering a decade of observations (see Table 1) to understand the variation of accretion and reflection parameters and predict the polarisation degree from the model-fitted accretion disc parameters.

3.2.1 Accretion-ejection based JeTCAF model

As the accreting matter moves closer to the BH its velocity increases and becomes supersonic, which may or may not form
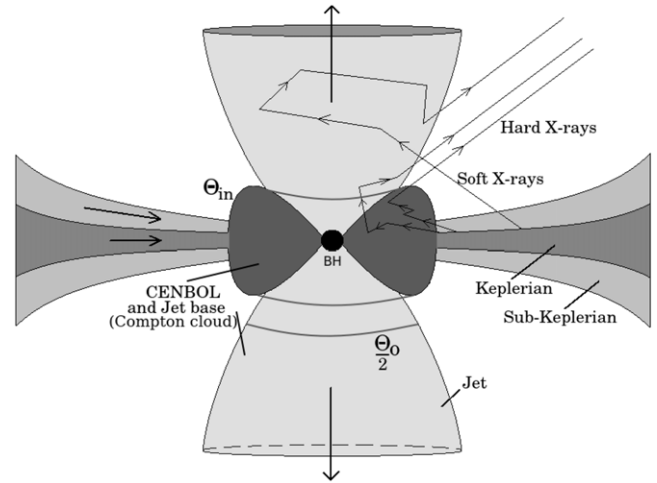

Figure 2. Illustration of the `JeTCAF` model. The Keplerian disc is residing at the equatorial plane while the sub-Keplerian halo component is above and below the equatorial plane, respectively. The deep grey inner region is the hot Compton cloud and the conical funnels above and below this region show the mass outflow or jet. The zig-zag arrows indicate the scattering of soft disc photons by different Comptonizing mediums. The figure is adapted from Mondal & Chakrabarti (2021).

shocks (Chakrabarti 1989) depending on the satisfaction of the Rankine-Hugoniot conditions. The location of the formation of the shock is known as the boundary layer of the corona. The same shocked region also drives jets/outflows and behaves as the base of the jet (Chakrabarti 1999). Therefore, we further fit the data using an accretion-ejection-based jet in a two-component advective flow model (or JeTCAF, Mondal & Chakrabarti 2021) to understand the accretion-ejection and polarisation behaviour of the source. The JeTCAF model is the updated version of TCAF model (Chakrabarti&Titarchuk 1995) that takes into account the spectral signature of jet or mass outflows. The model with flow geometry is illustrated in Fig. 2. The JeTCAF model takes into account radiation mechanisms at the base of the jet and the bulk motion effect by the outflowing jet on the emitted spectra in addition to the Compton scattering of soft disc photons by the hot electron cloud inside the corona. The JeTCAF model has six parameters, namely (i) the mass of the BH (M_{BH}), (ii) the Keplerian disc accretion rate ($\dot{m}_d$), (iii) the sub-Keplerian halo accretion rate ($\dot{m}_h$), (iv) the size of the dynamic corona or the location of the shock (X_s in $r_g = 2GM_{BH}/c^2$ unit), (v) the shock compression ratio (R), and (vi) the outflow/jet collimation factor (f_{col}), that is, the ratio of the solid angle subtended by the outflow to the inflow (Θ_o/Θ_{in}).

In general, an increase in $\dot{m}_d$ makes the spectrum softer as the increased number of soft photons from the disc cools the corona and lowers the outflow rate (Mondal, Chakrabarti, & Debnath 2014). While for increased $\dot{m}_h$ spectrum becomes harder as the corona is hotter and bigger, therefore, soft photons can gain more energy through scattering (Chakrabarti 1997; Mondal & Chakrabarti 2013). That also elevates the mass outflow rate. The increase in X_s also makes the spectrum harder as more hard photons from the hot corona contribute to it. In this model, the f_{col} parameter is incorporated to take into account the effect of outflows in addition to TCAF parameters. A higher value of this parameter implies that the jet is less collimated due to a higher outflowing angle, which makes the spectrum harder. As the mass
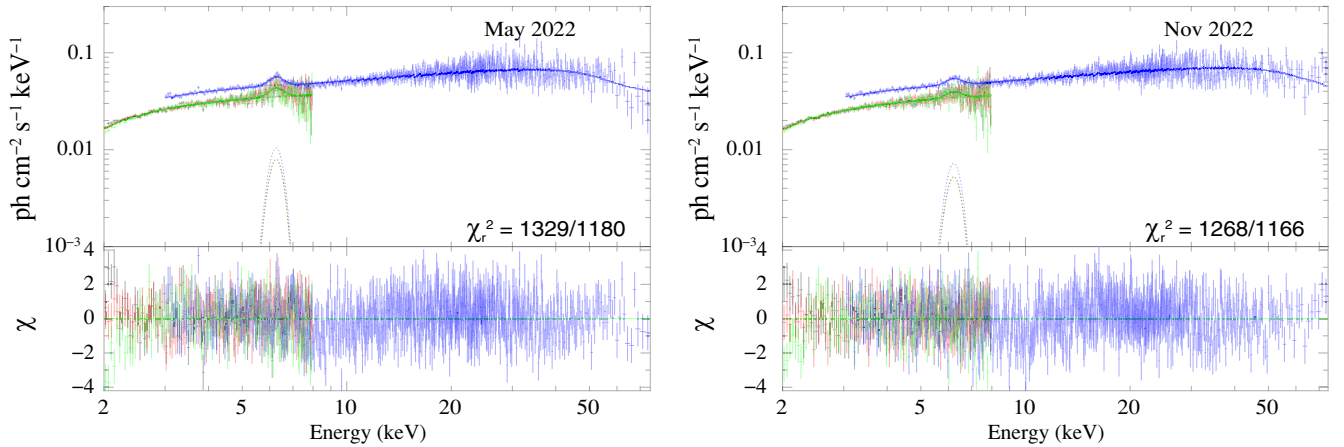
Figure 3. Joint spectral modelling of *IXPE* and *NuSTAR* data fitted using `JeTCAF` model in the energy band 2–79 keV. The left and right panels are for the epochs (I1+N1) and (I2+N2). The Fe Kα line $\sim$ 6.3 is fitted using `GAUSS` model as shown by dashed lines. The black, red, and green points correspond to *IXPE* data for all three DUs and the blue points correspond to *NuSTAR* data. See the text for details.

is a parameter, along with the accretion rates and corona parameters, the JeTCAF model has the potential to estimate the mass of the central SMBH as previously done for several BHs using TCAF, if there is no robust estimation beforehand (Iyer et al. 2015; Molla et al. 2017; Nandi, Chakrabarti, & Mondal 2019; Mondal et al. 2022). For the host galaxy absorption, we used the ZTBABS model. The full model reads in *XSPEC*[d] for *IXPE* and *NuSTAR* as TBABS*ZTBABS* (JeTCAF+GAUSS).

In Fig. 3, we show the model-fitted spectra of MCG-5-23-16 for the joint *IXPE* and *NuSTAR* observations. The Fe Kα line fitted well with a Gaussian line width of $\sim$ 0.3 keV for all observations. The Compton hump part of the spectra fitted with JeTCAF model is taken into account by the scattering of corona photons by the diverging outflow. The disc mass accretion rate in JeTCAF model varied minimally, whereas the halo accretion rate was nearly constant $\sim$ 0.4 $\dot{m}_{Edd}$ and the size of the corona changed significantly from $\sim$ 28 to 40 r_s. The model fit to all the epochs gives nearly a constant mass within errors of the central SMBH $\sim 2 \times 10^7$ M$_\odot$, consistent with previous estimations reported in the literature. However, if we freeze the mass to a known value of 2×10^7 M$_\odot$ from the literature, it will provide consistent fits. That will also reduce the errors noticeably in $\dot{m}_d$ and $\dot{m}_h$ and marginally in other parameters. For the joint epochs data (I1+N1 and I2+N2) fits, the N_H for the host galaxy absorption required in ZTBABS model is $2.0 - 2.2 \times 10^{22}$ cm^{-2}, while earlier *NuSTAR* epochs (N3-N7) required $N_H \sim 1.2 - 1.5 \times 10^{22}$ cm^{-2}. The high value of the f_{col} parameter implies that the outflow is not well collimated and the rate is high. The estimated outflow solid angle is $\sim 0.5\pi$. The JeTCAF model fitted parameters are summarised in Table 4.

From the JeTCAF model fitted parameters, we have estimated different physical quantities to understand the variation of polarisation with corona geometry and spectral flux. The height of the corona is basically the height of the shock, as the shock is the boundary layer of the corona. The height of the shock (h_{shk}) is estimated using (Debnath, Chakrabarti, & Mondal 2014), $h_{shk} = [\gamma(R-1)X_s^2/R^2]^{1/2}$, where, γ is the adiabatic index of the flow,

which is considered here as 5/3. The estimated h_{shk} varies in a range between $\sim 14 - 21\ r_s$.

The mass outflow rate ($\dot{m}_{out}$) is derived for an isothermal base of the jet (Chakrabarti 1999), which is given by,

$$\dot{m}_{out} = \dot{m}_{in} f_{col} f_0^{3/2} \frac{R}{4} \exp\left[\frac{3}{2} - f_0\right], \qquad (1)$$

where, $f_0 = \frac{R^2}{R-1}$ and $\dot{m}_{in}(= R\dot{m}_h + \dot{m}_d)$ is the total mass inflow rate. As the matter gets compressed at the shocked region by a factor of R, it changes the optical depth of the corona (see Chakrabarti & Titarchuk 1995; Modal et al. 2014). The estimated $\dot{m}_{out}$ varies between $0.14 \pm 0.03 - 0.20 \pm 0.03\ \dot{M}_{Edd}$ for this source, which is significant as was reported earlier in the literature (see, Braito et al. 2007). According to this model, as mentioned earlier, both corona and base of the jet behave as a Comptonizing medium. The radiation scattered by the corona or wind may exhibit significant polarisation. The unpolarised radiation from the central source scattered by the corona of radius X_s at height h_{shk} above the midplane of the disc will acquire a net fractional polarisation (Begelman & McKee 1983),

$$\Pi_{sc} = \frac{\sin^2 i[1 - 2(h_{shk}/X_s)^2]}{2[1 + 2(h_{shk}/X_s)^2] + [1 - 2(h_{shk}/X_s)^2]\sin^2 i}, \qquad (2)$$

where i is the disc inclination angle. As the above estimation uses only Thomson scattering as an approximation of Compton similar to JeTCAF model, thereby, the scattering conserves photon energy. Moreover, the Thomson scattering has no frequency dependence so it would preserve the incident spectrum for any energy bands including *IXPE* coverage. Therefore, for a given or well-estimated corona properties and disc inclination, one can estimate PD or vice-versa using Equation (2). Thereby, to shed light on the estimation of i from the polarisation measurement, we have calculated it from the observed upper limit of the PD in Marinucci et al. (2022), Tagliacozzo et al. (2023) and the broadband spectroscopic data fitted JeTCAF model parameters. Our estimated i ranges between 31°–35° during epochs I2 and I1 for given observed PDs. The rest of the *NuSTAR* epochs do not have polarisation data, thereby the measurement of observed PD values. However, we can predict the expected PDs by taking an average value of i (which is 33°) from I1 and I2 epochs and using it in Equation (2).

---

[d]At present the model is not publicly available in *XSPEC*, however, a preliminary version of the FITS file is in the testing phase which can be available soon upon request.

Table 4. Joint *IXPE* and *NuSTAR* data fitted model parameters are provided in this table. Here, M_{BH}, $\dot{m}_d$, $\dot{m}_h$, X_s, R, and f_{col} are the mass of the BH, disc and halo mass accretion rates, location of the shock or size of the corona, the shock compression ratio, and the outflow collimation factor respectively in JeTCAF model. N_H is the hydrogen column density in ZTBABS model. All data sets required GAUSS model for the Fe Kα line $\sim$ 6.3 keV of width σ_g given in the table.

Model	JeTCAF						ZTBABS	GAUSS	
Epoch	M_{BH}	$\dot{m}_d$	$\dot{m}_h$	X_s	R	f_{col}	N_H	σ_g	χ^2/dof
	$(10^7 M_\odot)$	$(10^{-2}\dot{m}_{Edd})$	$(\dot{m}_{Edd})$	(r_s)			$(10^{22}\ cm^{-2})$	(keV)	
I1+N1	2.0 ± 0.3	1.3 ± 0.2	0.41 ± 0.03	38.3 ± 4.4	4.91 ± 0.51	0.53 ± 0.07	2.21 ± 0.25	0.30 ± 0.03	1 329/1 180
I2+N2	2.1 ± 0.2	0.9 ± 0.1	0.40 ± 0.03	39.4 ± 3.4	4.36 ± 0.23	0.49 ± 0.04	2.04 ± 0.39	0.31 ± 0.04	1 268/1 166
N3	2.1 ± 0.2	1.2 ± 0.2	0.40 ± 0.02	28.2 ± 3.1	5.24 ± 0.38	0.45 ± 0.04	1.37 ± 0.11	0.27 ± 0.02	1 102/989
N4	1.9 ± 0.2	1.3 ± 0.1	0.41 ± 0.03	34.9 ± 3.9	5.19 ± 0.32	0.49 ± 0.05	1.22 ± 0.09	0.31 ± 0.03	864/768
N5	2.0 ± 0.1	1.3 ± 0.1	0.41 ± 0.02	29.9 ± 2.1	5.28 ± 0.42	0.47 ± 0.03	1.49 ± 0.15	0.31 ± 0.02	1 029/928
N6	2.1 ± 0.1	1.1 ± 0.1	0.41 ± 0.04	39.8 ± 4.6	4.98 ± 0.37	0.54 ± 0.03	1.27 ± 0.07	0.35 ± 0.03	983/930
N7	2.0 ± 0.1	1.3 ± 0.1	0.42 ± 0.02	37.9 ± 2.8	5.06 ± 0.30	0.53 ± 0.04	1.14 ± 0.15	0.27 ± 0.02	609/570

Table 5. Estimated and observed polarisation and corona properties of MCG-5-23-16. The 3–79 keV band flux is in units of 10^{-10} erg cm^{-2} s^{-1}. Here, [a,b] denotes the references to Marinucci et al. (2022) and Tagliacozzo et al. (2023). In the first two rows, [c] denotes the estimation of i from the observed upper limits of PD, while the expected PDs in column 5 are calculated using JeTCAF model geometry and for $i = 33°$, which is an average of the estimates in the first two epochs (35° and 31° respectively). The column 8 denotes the estimations of PD for a given angle of 45°, which is considered from the literature. The last two columns stand for the same estimation of PD for a given i, which is obtained from relxillCp model and using the geometry from JeTCAF model.

Epoch	$\dot{m}_{out}$	h_{shk}	$F_{3-79\ keV}$	PD(%)		$i°$	PD(%)	PD(%)	$i°$
	$(\dot{m}_{Edd})$	(r_s)		Estm.	Obs.[a,b]	JeTCAF	Estm.	Estm.	relxillCp
I1+N1	0.19 ± 0.04	19.9 ± 2.5	2.75 ± 0.02	4.2	≤ 4.7	35^c	6.9	4.9	35.9
I2+N2	0.20 ± 0.03	21.4 ± 1.9	2.84 ± 0.02	3.7	≤ 3.3	31^c	6.1	3.4	31.4
N3	0.14 ± 0.03	14.3 ± 1.7	2.66 ± 0.03	4.5	–	33	7.4	7.4	44.8
N4	0.16 ± 0.02	17.8 ± 2.1	2.53 ± 0.01	4.5	–	33	7.3	5.8	38.6
N5	0.15 ± 0.02	15.1 ± 1.2	2.30 ± 0.02	4.6	–	33	7.5	6.0	39.1
N6	0.19 ± 0.03	20.6 ± 2.5	3.09 ± 0.02	4.3	–	33	7.0	5.9	39.9
N7	0.19 ± 0.02	19.5 ± 1.6	2.87 ± 0.02	4.4	–	33	7.2	5.7	38.8

Our estimation is a bit lower compared to the estimations reported in the literature, however, falls in the range estimated using reflection models (see the next section). Therefore, we have further estimated the PD values for $i = 45°$ as a comparison with the literature. All estimated PD values are given in Table 5. The spectral flux given in the table is calculated using *flux err* command in *XSPEC* for the energy band 2–79 keV.

The left panel of Fig. 4 shows the variation of PD with the radial distance of the corona. The red circles are the PD values estimated using the model fitted h_{shk} and X_s parameters for a given $i = 33°$, which is the average of disc inclination angles estimated from the upper limit of the observed PD values reported in Tagliacozzo et al. (2023). For a corona of $< 35\ r_s$, the PD was nearly constant and it decreased when the corona size increased. A similar profile has been observed (middle panel of Fig. 4) for the height of the corona, which is quite expected as a bigger corona indicates a hotter electron cloud and more puffed up in the vertical direction. Our estimated PD variation with corona geometry is in accord with the simulation results performed by Schnittman & Krolik (2010) for a spherical geometry of the corona. The right panel of Fig. 4 shows the PD variation with estimated spectral flux, which shows a negative correlation as well. The variations of PD values estimated for $i = 45°$ with the corona properties and model flux

are shown by green triangles in all three panels of Fig. 4. For the estimation, we used the corona geometry obtained from JeTCAF model fits. The estimated PD values are higher by nearly a factor of two than the observed and JeTCAF model estimations. A more spherical corona might be required for the same disc inclination to get a lower value of PD which can match with observations.

3.2.2 Reflection based pexrav and relxillCp models

Further, we have used reflection-based pexrav and relxillCp models to fit the joint and individual spectra to constrain different reflection parameters. The models reads in XSPEC as TBABS*ZTBABS*(GAUSS+pexrav) and TBABS* ZTBABS*relxillCp, and a CONST component for the first two epochs. For both model fittings, we set the abundances to their Solar value. First, we fit the data using pexrav model, where the reflection parameter (R_{ref}) varied between $0.46 \pm 0.14 - 0.69 \pm 0.22$, the powerlaw photon index $1.78 \pm - 1.94 \pm 0.03$. The FeKα line fitted ~ 6.3 keV with width σ_g as tabulated in Table 6. From this model fit, we could constrain the cutoff energy ranges between 130–184 keV. These values were used during fitting using relxillCp model. To constrain the disc inclination angle (i), we put a range of $0.6 < i < 0.9$.
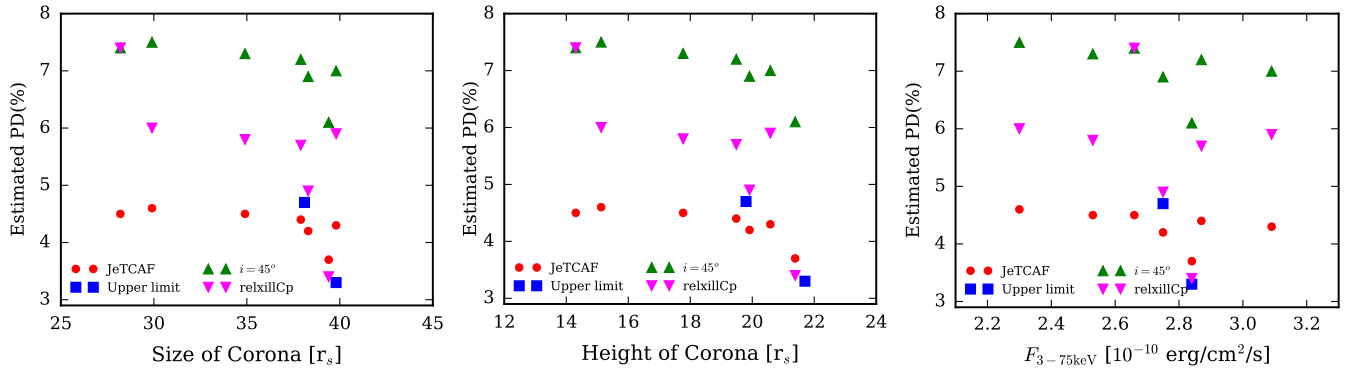
Figure 4. Dependence of PD with the geometry of the Comptonizing corona in `JeTCAF` model. The left and middle panels show the PD variation with the radial distance and height of the corona, while the right panel shows the PD variation with the observed flux in the 3–79 keV band. The red circles show the predicted PD, estimated using spectral model fitted accretion parameters, and the blue squares show the observed upper limit in PD measurement. The magenta upside down triangles and green triangles show the PD estimations from `relxillCp` model fitted disc inclination and for a given inclination of 45°.

For some epochs (N3-N5), the i value is pegged at the lower limit, therefore, we could not constrain its value. However, the other epochs returned the inclination angle value between 35°–54°. The N_H values for the first two epochs are between 2.25 and 2.50×10^{22} cm^{-2}, while for the epochs N3-N7 it is between 1.60–1.86×10^{22} cm^{-2}, showing a similar trend as obtained in `JeTCAF` model.

The relativistic reflection model (`relxill`) has several variants, including `relxillCp`, which we have used for our purposes. This model takes into account the relativistic disc reflection component and `NTHCOMP` (Zdziarski, Johnson, &Magdziarz 1996; Życki, Done, & Smith 1999) thermal Comptonization continuum component. The `relxillCp` model has fourteen parameters out of which two are abundances which we set to their Solar values. If we keep all parameters free, that will give more degenerate values of the parameters and most of the parameters can not be well-constrained. Therefore, before fitting the data we make an educated choice of some of the parameters as was done by several authors in the literature (Barua et al. 2023; Serafinelli et al. 2023, and references therein). From the rest of the parameters, we choose non-rotating BH at present, as there is no reporting of the spin parameter for this system. We tried to fit the data by keeping the spin parameter free, and it was always taking the upper hard limit of 0.998. Such a high spin can not be explained from the present data sets as the source evidenced a stable accretion disc being truncated at a larger radius (see Serafinelli et al. 2023, for more details). This task prompted us to set a and R_{in} parameters to 0 and 6 r_g in this work. The outer edge of the disc, R_{out} is set to 1 000 r_g. The parameter R_{br} determines a break radius that separates two regimes with different emissivity profiles and is set to 38 r_g, following the previously reported results in the literature and `JeTCAF` model fitted results. We fixed the first emissivity index (*index1*) to 3.0 and put a range for the *index2* (q_2) between 0.1–4. We set kT_e fixed to values obtained from `pexrav` model fit. The remaining six parameters i, Γ, ionisation index (log ξ), density (N), and R_{ref} are set free to vary.

Fig. 5 shows the `relxillCp` model fitted the joint spectra for the epochs May (left panel) and November (right panel). The model fits the data well and the residual is shown in the bottom panels. Using the `relxillCp` model, we could well-constrain the disc inclination i between $31.4 \pm 7.9 - 44.8 \pm 7.3$ and the Γ was nearly constant across all epochs with value between

1.90 ± 0.01–1.99 ± 0.02. The estimated value of i from `JeTCAF` model as given in Table 5 falls within the range of values obtained from `relxillCp` model. This range of inclination angle is also in accord with the estimation in the literature (Marinucci et al. 2022; Serafinelli et al. 2023). The emissivity index (q_2) is pegged at 0.1 for all epochs except the epoch N6, for which we obtained a value 1.87 ± 0.40. Our model fits yield ionisation parameter log $\xi \leq 1.6$, which infers that the distant reflecting material is not highly ionised. The obtained density of the matter (N) at R_{in} is high, varies between $10^{18-19.6}$ cm^{-3}, and the reflection fraction R_{ref} between $0.5 - 0.8$, which is relatively low. Both reflection model fitted R_{ref} are in close agreement with each other. All reflection model parameters are given in Table 6. We have further estimated the PD values using `relxillCp` model fitted i values. The results are summarised in Table 5. The variations of PD estimated using `relxillCp` model fitted i values are shown by upside-down magenta triangles in all three panels of Fig. 4. It is noticeable that these PD values fall in between the observed and for $i = 45°$ estimations.

to appear in While using two reflection-based models to the same set of data, both models fit the data equally well provided some marginal changes in χ^2 values. However, from the `pexrav` model we could not constrain the i parameter, provided a broad range. The `relxillCp` could constrain the i values which are in agreement with the literature, and we could use them to compare the observed PD measurement. Since the `pexrav` model could constrain the E_{cut}, we could use them in `relxillCp` model. Other common parameters (Γ and R_{ref}) obtained from the fit in both models are quite similar. We note that, the `relxillCp` model takes into account the ionised reflection, ionisation, and relativistic effects, could constrain the required parameter and, therefore more favourable for the present study, compared to the `pexrav` model.

4. Discussions and conclusions

In this work, we have performed the spectro-polarimetric analysis of the Seyfert galaxy MCG-5-23-16 to understand the polarisation properties and the X-ray emitting corona using two epochs of data from *IXPE* and a decade of observations from *NuSTAR*. Our model-independent analysis poses the PD with an upper limit of $\leq 3.8\%$, while the model-dependent estimates give PD

Table 6. Joint *IXPE* and *NuSTAR* data fitted reflection model parameters are provided in this table. All data sets required `GAUSS` model for the Fe Kα line ∼ 6.3 keV of width σ_g given in the table during `pexrav` model fitting. During both `relxillCp` and `pexrav` model fitting both abundances are set to Solar value. Here, ^{p} and ^{f} denote the pegged and frozen values of the parameters.

| Models	Parameters	Epochs						
		I1+N1	I2+N2	N3	N4	N5	N6	N7
`ZTBABS`	N_H (10^{22} cm^{-2})	2.50 ± 0.17	2.25 ± 0.15	1.60 ± 0.23	1.58 ± 0.34	1.86 ± 0.26	1.82 ± 0.24	1.86 ± 0.28
`GAUSS`	σ_g (keV)	0.18 ± 0.03	0.19 ± 0.04	0.18 ± 0.02	0.18 ± 0.03	0.22 ± 0.02	0.24 ± 0.02	0.17 ± 0.05
`pexrav`	Γ	1.94 ± 0.03	1.89 ± 0.03	1.78 ± 0.02	1.83 ± 0.04	1.81 ± 0.03	1.86 ± 0.03	1.88 ± 0.06
	E_c (keV)	180.5 ± 30.6	184.3 ± 33	135.5 ± 13.9	152.6 ± 27.1	145.3 ± 17.8	129.6 ± 13.9	184.3 ± 31.6
	R_{ref}	0.58 ± 0.22	0.46 ± 0.21	0.46 ± 0.14	0.54 ± 0.23	0.58 ± 0.17	0.56 ± 0.16	0.69 ± 0.08
	cos (i)	0.81 ± 0.18	0.82 ± 0.23	0.6^p	0.6^p	0.6^p	0.74 ± 0.26	0.69 ± 0.22
Fit statistics	χ^2/dof	1 260/1 182	1 198/1 169	1 020/987	830/869	945/926	877/929	567/571
`ZTBABS`	N_H (10^{22} cm^{-2})	2.91 ± 0.16	2.34 ± 0.14	1.93 ± 0.19	1.98 ± 0.32	1.95 ± 0.40	1.69 ± 0.16	1.78 ± 0.28
`relxillCp`	i (°)	35.9 ± 10.7	31.4 ± 7.9	44.8 ± 7.3	38.6 ± 8.8	39.1 ± 7.4	39.9 ± 7.5	38.8 ± 9.4
	q_2	0.1^p	0.1^p	0.1^p	0.1^p	0.1^p	1.87 ± 0.40	0.1^p
	Γ	1.99 ± 0.02	1.93 ± 0.02	1.90 ± 0.01	1.95 ± 0.01	1.94 ± 0.01	1.95 ± 0.01	1.94 ± 0.02
	$\log \xi$	0.93 ± 0.34	1.28 ± 0.18	1.14 ± 0.10	0.57 ± 0.44	0.70 ± 0.33	1.22 ± 0.18	1.56 ± 0.38
	N(cm^{-3})	18.05 ± 0.45	18.19 ± 0.29	19.57 ± 0.29	18.07 ± 0.20	18.16 ± 0.28	19.41 ± 0.30	18.27 ± 0.57
	kT_e^f (keV)	181	184	136	153	145	130	184
	R_{ref}	0.61 ± 0.01	0.48 ± 0.08	0.51 ± 0.09	0.63 ± 0.08	0.75 ± 0.13	0.60 ± 0.07	0.67 ± 0.19
Fit statistics	χ^2/dof	1251/1 181	1 197/1 168	1 022/988	822/870	943/927	896/930	569/572
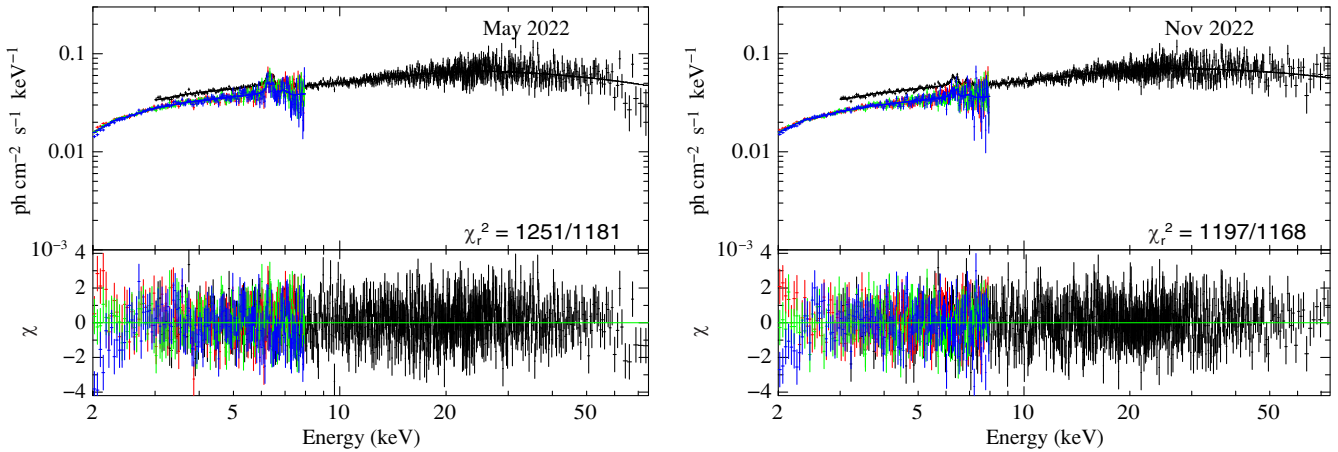
Figure 5. Same as Fig. 3 but using `relxillCp` model. See the text for details.

$1.08 \pm 0.66\%$ and PA $55.6° \pm 19.1°$ using simultaneous data fitting of I1 and I2, which are in accord with the previous studies within error bar (Marinucci et al. 2022; Tagliacozzo et al. 2023).

The joint *IXPE* and *NuSTAR* broadband spectroscopic data fitted using JeTCAF model gives the estimate of disc mass accretion rate to the central SMBH which is $\leq 0.013 \ \dot{m}_{Edd}$, while the halo accretion rate is $\leq 0.4 \ \dot{m}_{Edd}$. The location of the shock changed from 28 to 40 r_s and the shock compression ratio varied between 4.4–5.3. Relatively high values of jet/outflow collimation factor indicate that the outflow is not well-collimated. The previous studies reported that the source showed significant mass outflow, here we estimated the mass outflow rate ∼0.14–0.20 $\dot{m}_{Edd}$ from the spectral model fitted parameters. Since mass outflow

carries thermal energy from the hot corona, its geometry changes (Chakrabarti 1999; Mondal et al. 2014). Therefore, the final best-fit corona geometry which is used to estimate the expected PD has the effect of mass outflows. Hence, studying polarisation using the disc-corona-outflows model is crucial to get a consistent picture of a system, which has been done in this work. Since the model directly fits the data using corona geometry and estimates expected i using observed quantities, such estimations might be more favourable.

We have further fitted the data using `pexrav` and `relxillCp` models to constrain the reflection properties and disc inclination (i). We found that the reflection fraction, $R_{ref} < 0.8$ which agrees with previous studies, and the photon index Γ was also consistent

in both models. In `pexrav` model, we could constrain *i* for some epochs, and for some epochs fits were trending towards very high inclination. However, using `relxillCp` we could constrain *i* for all epochs which put a range $\sim 31°–45°$, which is in agreement with the previous studies. Therefore, the `relxillCp` is a more favourable reflection model for the present data sets compared to `pexrav`. Given these values of *i* from `relxillCp` model, we have estimated the expected PD to be 3.4–6.0%, which is comparatively similar to higher than the observed PD.

The scattering of photons inside the Comptonizing corona or outflow can induce significant polarisation as discussed earlier. Therefore, we used it to further estimate the disc inclination for a given corona geometry from `JeTCAF` model, mainly its radial distance and height. Using the upper limit of polarisation measurement, we have estimated the disc inclination $\sim 35°$ using observations in May 2022 (I1+N1) and $\sim 31°$ in November 2022 (I2+N2). After taking an average of these two estimates, we further use it to determine the expected polarisation during the epochs N3-N7. The estimated PD decreases with increasing the corona geometry at different epochs (see Fig. 4). We note that the expected *i* estimated using the `JeTCAF` geometry for the simultaneous data sets nicely matches with the `relxillCp` model fitted *i*. We have further estimated the expected PDs using *i* from `relxillCp` model and also considering *i* to be 45° are shown in all three panels of Fig. 4 for a comparative study. These values are above the presently observed upper limit which may suggest that the disc inclination predicted from `JeTCAF` and obtained from `relxillCp` model is more reliable. However, if such a high PD is expected, that can be possibly measured in the future with broadband polarimetry using joint *IXPE* and *XPoSat*, which may provide higher inclination, require a further study. Our study not only relates the polarisation with the accretion flow properties but also can predict expected polarisation. The current model prescription can be applied to other Seyfert galaxies to study their X-ray polarisation in connection with the accretion-ejection properties, where polarisation could be due to reflection (NGC 4151; Gianolli et al. 2023) or outflowing jet (IC 4329A; Ingram et al. 2023; Pal et al. 2023), which will be addressed in elsewhere. Additionally, the current modelling can be applied to *XPoSat* observations of this source and other potential candidates in the future.

Data availability statement. Data used in this work are publicly available in NASA's HEASARC archive. The `JeTCAF` model (Mondal & Chakrabarti 2021) is incorporated in *XSPEC* directly using `initpackage` command, which is not public yet. However, the preliminary version of the FITS file is in a testing phase and can be available soon upon request or on GitHub.[e]

References

Arnaud, K. A. 1996, in Astronomical Data Analysis Software and Systems V, ed. G. H. Jacoby, & J. Barnes, 101, 17. Astronomical Society of the Pacific Conference Series.

Baldini, L., et al. 2022, SoftwareX, 19, 101194. https://doi.org/10.1016/j.softx.2022.101194. arXiv: 2203.06384 [astro-ph.IM].

Balestra, I., Bianchi, S., & Matt, G. 2004, A&A, 415, 437. https://doi.org/10.1051/0004-6361:20030211. arXiv: astro-ph/0311316 [astro-ph].

Baloković, M., et al. 2015, ApJ, 800, 62. https://doi.org/10.1088/0004-637X/800/1/62. arXiv: 1412.5978 [astro-ph.HE].

Barua, S., Adegoke, O. K., Misra, R., Pawar, P., Jithesh, V., & Medhi, B. J. 2023, ApJ, 958, 46. https://doi.org/10.3847/1538-4357/acf464. arXiv: 2308.11552 [astro-ph.HE].

Beckmann, V., Courvoisier, T. J.-L., Gehrels, N., Lubiński, P., Malzac, J., Petrucci, P.-O., Shrader, C. R., & Soldi, S. 2008, A&A, 492, 93. https://doi.org/10.1051/0004-6361:200810674. arXiv: 0810.3774 [astro-ph].

Begelman, M. C., & McKee, C. F. 1983, ApJ, 271, 89. https://doi.org/10.1086/161179.

Beheshtipour, B., Krawczynski, H., & Malzac, J. 2017, ApJ, 850, 14. https://doi.org/10.3847/1538-4357/aa906a. arXiv: 1710.00247 [astro-ph.HE].

Braito, V., et al. 2007, ApJ, 670, 978. https://doi.org/10.1086/521916. arXiv: 0707.2950 [astro-ph].

Chakrabarti, S., & Titarchuk, L. G. 1995, ApJ, 455, 623. https://doi.org/10.1086/176610. arXiv: astro-ph/9510005 [astro-ph].

Chakrabarti, S. K. 1989, ApJ, 347, 365. https://doi.org/10.1086/168125.

Chakrabarti, S. K. 1997, ApJ, 484, 313. https://doi.org/10.1086/304325. arXiv: astro-ph/9706001 [astro-ph].

Chakrabarti, S. K. 1999, A&A, 351, 185. arXiv: astro-ph/9910014 [astro-ph].

Connors, P. A., Piran, T., & Stark, R. F. 1980, ApJ, 235, 224. https://doi.org/10.1086/157627.

Dauser, T., Garcia, J., Parker, M. L., Fabian, A. C., & Wilms, J. 2014, MNRAS, 444, L100. https://doi.org/10.1093/mnrasl/slu125. arXiv: 1408.2347 [astro-ph.HE].

Debnath, D., Chakrabarti, S. K., & Mondal, S. 2014, MNRAS, 440, L121. https://doi.org/10.1093/mnrasl/slu024. arXiv: 1402.0989 [astro-ph.HE].

Dewangan, G. C., Griffiths, R. E., & Schurch, N. J. 2003, ApJ, 592, 52. https://doi.org/10.1086/375640. arXiv: astro-ph/0304037 [astro-ph].

Di Marco, A., et al. 2022, AJ, 163, 170. https://doi.org/10.3847/1538-3881/ac51c9. arXiv: 2202.01093 [astro-ph.IM].

Done, C., Gierliński, M., & Kubota, A. 2007, A&ARv, 15, 1. https://doi.org/10.1007/s00159-007-0006-1. arXiv: 0708.0148 [astro-ph].

Dovčiak, M., Muleri, F., Goosmann, R. W., Karas, V., & Matt, G. 2008, MNRAS, 391, 32. https://doi.org/10.1111/j.1365-2966.2008.13872.x. arXiv: 0809.0418 [astro-ph].

Ferruit, P., Wilson, A. S., & Mulchaey, J. 2000, ApJS, 128, 139. https://doi.org/10.1086/313379.

Garcia, J., et al. 2014, ApJ, 782, 76. https://doi.org/10.1088/0004-637X/782/2/76. arXiv: 1312.3231 [astro-ph.HE].

Gianolli, V. E., et al. 2023, MNRAS, 523, 4468. https://doi.org/10.1093/mnras/stad1697. arXiv: 2303.12541 [astro-ph.GA].

Haardt, F., & Maraschi, L. 1993, ApJ, 413, 507. https://doi.org/10.1086/173020.

Harrison, F. A., et al. 2013, ApJ, 770, 103. https://doi.org/10.1088/0004-637X/770/2/103. arXiv: 1301.7307 [astro-ph.IM].

HI4PI Collaboration, et al. 2016, A&A, 594 A116. https://doi.org/10.1051/0004-6361/201629178. arXiv: 1610.06175 [astro-ph.GA].

Ingram, A., et al. 2023, MNRAS, 525, 5437. https://doi.org/10.1093/mnras/stad2625. arXiv: 2305.13028 [astro-ph.HE].

[e]https://github.com/santanumondal87/JeTCAF-A-package-for-X-ray-spectral-fitting-of-black-holes-across-mass-scale.

Iyer, N., Nandi, A., & Mandal, S. 2015, ApJ, 807, 108. https://doi.org/10.1088/0004-637X/807/1/108. arXiv: 1505.02529 [astro-ph.HE].

Joye, W. A., & Mandel, E. 2003, in Astronomical Data Analysis Software and Systems XII, ed. H. E. Payne, R. I. Jedrzejewski, & R. N. Hook, 295, 489. Astronomical Society of the Pacific Conference Series.

Kalberla, P. M. W., Burton, W. B., Hartmann, D., Arnal, E. M., Bajaja, E., Morras, R., & Pöppel, W. G. L. 2005, A&A, 440, 775. https://doi.org/10.1051/0004-6361:20041864. arXiv: astro-ph/0504140 [astro-ph].

Kislat, F., Clark, B., Beilicke, M., & Krawczynski, H. 2015, APh, 68, 45. https://doi.org/10.1016/j.astropartphys.2015.02.007. arXiv: 1409.6214 [astro-ph.IM].

Li, L.-X., Narayan, R., & McClintock, J. E. 2009, ApJ, 691, 847. https://doi.org/10.1088/0004-637X/691/1/847. arXiv: 0809.0866 [astro-ph].

Liu, V., Zoghbi, A., & Miller, J. M. 2024, ApJ, 963, 38. https://doi.org/10.3847/1538-4357/ad18c8. arXiv: 2312.16354 [astro-ph.HE].

Magdziarz, P., & Zdziarski, A. A. 1995, MNRAS, 273, 837. https://doi.org/10.1093/mnras/273.3.837.

Marinucci, A., et al. 2022, MNRAS, 516, 5907. https://doi.org/10.1093/mnras/stac2634. arXiv: 2207.09338 [astro-ph.HE].

Mattson, B. J., & Weaver, K. A. 2004, ApJ, 601, 771. https://doi.org/10.1086/380502. arXiv: astro-ph/0310468 [astro-ph].

Molina, M., Bassani, L., Malizia, A., Stephen, J. B., Bird, A. J., Bazzano, A., & Ubertini, P. 2013, MNRAS, 433, 1687. https://doi.org/10.1093/mnras/stt844. arXiv: 1305.2722 [astro-ph.HE].

Molla, A. A., Chakrabarti, S. K., Debnath, D., & Mondal, S. 2017, ApJ, 834, 88. https://doi.org/10.3847/1538-4357/834/1/88. arXiv: 1611.01266 [astro-ph.HE].

Mondal, S., Adhikari, T. P., Hryniewicz, K., Stalin, C. S., & Pandey, A. 2022, A&A, 662, A77. https://doi.org/10.1051/0004-6361/202243084. arXiv: 2204.02133 [astro-ph.HE].

Mondal, S., & Chakrabarti, S. K. 2013, MNRAS, 431, 2716. https://doi.org/10.1093/mnras/stt361.

Mondal, S., & Chakrabarti, S. K. 2021, ApJ, 920, 41. https://doi.org/10.3847/1538-4357/ac14c2.

Mondal, S., Chakrabarti, S. K., & Debnath, D. 2014, Ap&SS, 353, 223. https://doi.org/10.1007/s10509-014-2008-6. arXiv: 1406.1878 [astro-ph.HE].

Nandi, P., Chakrabarti, S. K., & Mondal, S. 2019, ApJ, 877, 65. https://doi.org/10.3847/1538-4357/ab1d62. arXiv: 1905.02147 [astro-ph.HE].

Onori, F., et al. 2017, MNRAS, 468, L97. https://doi.org/10.1093/mnrasl/slx032. arXiv: 1703.05167 [astro-ph.GA].

Pal, I., Stalin, C. S., Chatterjee, R., & Agrawal, V. K. 2023, JApA, 44, 87. https://doi.org/10.1007/s12036-023-09981-5. arXiv: 2305.09365 [astro-ph.HE].

Ponti, G., Papadakis, I., Bianchi, S., Guainazzi, M., Matt, G., Uttley, P., & Bonilla, N. F. 2012, A&A, 542, A83. https://doi.org/10.1051/0004-6361/201118326. arXiv: 1112.2744 [astro-ph.HE].

Reeves, J. N., et al. 2007, PASJ, 59, 301. https://doi.org/10.1093/pasj/59.sp1.S301. arXiv: astro-ph/0610434 [astro-ph].

Schnittman, J. D., & Krolik, J. H. 2010, ApJ, 712, 908. https://doi.org/10.1088/0004-637X/712/2/908. arXiv: 0912.0907 [astro-ph.HE].

Serafinelli, R., et al. 2023, MNRAS, 526, 3540. https://doi.org/10.1093/mnras/stad2801. arXiv: 2309.06092 [astro-ph.HE].

Strohmayer, T. E. 2017, ApJ, 838, 72. https://doi.org/10.3847/1538-4357/aa643d. arXiv: 1703.00949 [astro-ph.IM].

Sunyaev, R. A., & Titarchuk, L. G. 1980, A&A, 500, 167.

Sunyaev, R. A., & Titarchuk, L. G. 1985, A&A, 143, 374.

Tagliacozzo, D., et al. 2023, MNRAS, 525, 4735. https://doi.org/10.1093/mnras/stad2627. arXiv: 2305.10213 [astro-ph.HE].

Tamborra, F., Matt, G., Bianchi, S., & Dovčiak, M. 2018, A&A, 619, A105. https://doi.org/10.1051/0004-6361/201732023. arXiv: 1808.07399 [astro-ph.HE].

Veron, P., Lindblad, P. O., Zuiderwijk, E. J., Veron, M. P., & Adam, G. 1980, A&A, 87, 245.

Weaver, K. A., & Reynolds, C. S. 1998, ApJL, 503, L39. https://doi.org/10.1086/311527. arXiv: astro-ph/9806168 [astro-ph].

Weaver, K. A., Yaqoob, T., Mushotzky, R. F., Nousek, J., Hayashi, I., & Koyama, K. 1997, ApJ, 474, 675. https://doi.org/10.1086/303488.

Wegner, G., et al. 2003, AJ, 126, 2268. https://doi.org/10.1086/378959. arXiv: astro-ph/0308357 [astro-ph].

Weisskopf, M. C., et al. 2016, in Space Telescopes and Instrumentation 2016: Ultraviolet to Gamma Ray, ed. J.-W. A. den Herder, T.-d. Takahashi, & M. Bautz, 9905:990517. Society of Photo-Optical Instrumentation Engineers (SPIE) Conference Series. https://doi.org/10.1117/12.2235240.

Wilms, J., Allen, A., & McCray, R. 2000, ApJ, 542, 914. https://doi.org/10.1086/317016. arXiv: astro-ph/0008425 [astro-ph].

Zdziarski, A. A., Johnson, W. N., & Magdziarz, P. 1996, MNRAS, 283, 193. https://doi.org/10.1093/mnras/283.1.193. arXiv: astro-ph/9607015 [astro-ph].

Zoghbi, A., et al. 2017, ApJ, 836, 2. https://doi.org/10.3847/1538-4357/aa582c. arXiv: 1701.02309 [astro-ph.HE].

Życki, P. T., Done, C., & Smith, D. A. 1999, MNRAS, 309, 561. https://doi.org/10.1046/j.1365-8711.1999.02885.x. arXiv: astro-ph/9904304 [astro-ph].